Optimal Observer-Based Pressure Sensor Placement for Rigid Sails ⋆

Sean Smith * **Emmanuel Witrant** * **Ya-Jun Pan** **

* *Université Grenoble Alpes, CNRS, GIPSA-lab, 38000, Grenoble, France (e-mail: sean.smith@univ-grenoble-alpes.fr, emmanuel.witrant@univ-grenoble-alpes.fr).*
** *Dalhousie University, ACM-lab, Halifax, Nova Scotia, B3H 4R2, Canada (e-mail: yajun.pan@dal.ca)*

Abstract: This paper investigates the optimal placement of pressure sensors for observer-based feedback on rigid domains, with a particular focus on rigid sails. Existing computational fluid dynamics (CFD) studies, supported by experimental validation, have shown promising results in analyzing sail aerodynamics using pressure sensors. Building on these developments, this study adapts the General Pressure Equation (GPE) into a linearized form, close to quasi-steady conditions, for pressure sensor placement analysis. Based on this model, an observer-based closed-loop strategy for optimal sensor placement is developed. A Lagrangian method is proposed to establish local optimality conditions in the infinite-dimensional setting without relying on reduced-order (lumped) models. The proposed strategy directly considers the state estimation efficiency within the optimal sensor placement process. The efficiency of the method to estimate the pressure field is illustrated by simulation results on a rigid sail with a symmetric profile and by experimental results on the jib (flexible) sail of a 6 m sailboat.

Keywords: Optimal sensor placement, partial differential equation (PDE) observers, rigid sails.

1. INTRODUCTION

The automatic control of sails has gained significant attention with the advent of autonomous sailboats. An overview by Tipsuwan et al. (2023) examines both modeling and control strategies: most approaches rely on wing or thin-airfoil theory to model aerodynamic forces, neglecting the underlying flow dynamics. While these simplifications enable model-based control, they can lead to suboptimal control performance and limited real-time applicability to account for unsteady dynamics.

Computational fluid dynamics (CFD) studies have provided a deeper insight into sail aerodynamics. For instance, Viola et al. (2013) showed that surface pressure measurements capture richer flow information than integrated force data, particularly for identifying flow separation, which is critical for sail efficiency. Moreover, correlations between lift-to-drag ratio and angle of attack were established from pressure distributions, indicating that maximizing drive force could be achieved through pressure-based control, provided that the pressure field is well characterized. Further work by Bot et al. (2014) reinforced these findings using a dense array of pressure probes to study flow separation, highlighting that rigid sails offer improved controllability over flexible ones, as pressure probe integration is more practical and pressure feedback is less distorted by surface deformation.

While CFD has made substantial progress in reconciling numerical simulations with experimental observations, the integration of CFD-based flow analysis, automatic sail control, and experimental implementation remains limited. Data-driven methods (Zhou et al. (2021)) and machine learning approaches (Zhang et al. (2025)), typically relying on lumped reduced-order models, have advanced flow and pressure estimation. Nonetheless, theoretical formulations derived directly in the infinite-dimensional setting remain underexplored. This gap arises because, in the incompressible Navier–Stokes equations, pressure is not explicitly governed by its own evolution equation and can only be obtained by a complex set of coupled, nonlinear, partial differential equations (PDEs). Recent studies by Toutant (2018) proposed pressure evolution models under isothermal and low–Mach-number conditions, opening new directions for mathematical analysis, state estimation, and control design.

Building on these experimental and computational findings, flow sensors offer an effective means of characterizing the surface pressure distribution at specific locations over aerodynamic bodies. For CFD analysis or automatic control applications, however, it is often necessary to reconstruct the full pressure field. Le Pelley et al. (2012) combined pressure sensors with a vision system and pressure measurement extrapolation for force feedback, placing sensors based on upwind sail distribution plots, while Rossetti et al. (2011) developed a wireless capacitive sensor system for sails and used simulations and experiments to

⋆ This work is supported by the Natural Sciences and Engineering Research Council (NSERC) of Canada, the France Canada Research Fund (FCRF), the Conseil National des Universités, and the French National Research Agency in the framework of the "Investissements d'avenir" program (ANR-15-IDEX-02).

assess sensor performance under applied pressures. However, these frameworks do not address optimal sensor placement or observer design. Pressure reconstruction can be achieved through the use of an observer (Luenberger (1971)). As a preliminary step toward observer-based estimation and control, the optimal placement of pressure sensors thus becomes a key prerequisite.

The problem of optimal sensor placement has been addressed by many works, with a large variety of methods that mostly differ in terms of reference model and performance criterion. Open-loop formulations aim to enhance observability through observability Gramians (Wrobel and Meurer (2021); Summers and Lygeros (2014)) and the $\mathcal{H}_2$ norm (Armaou and Demetriou (2014)), typically within reduced-order or truncated models. Related PDE-based approaches have also introduced eigenanalysis-inspired observability metrics for finite-dimensional modal systems. Further examples include proper orthogonal decomposition (POD) approaches (Meinicke and Cesnik (2025)), which estimated in-flight aerodynamic loads using internal strain and temperature sensors, with efforts to reconstruct pressure fields.

However, optimizing based solely on open-loop metrics often relies on state information extracted at a limited number of nodes or modes from a reduced-order model. Such formulations may yield sensor configurations that perform well within the reduced subspace but exhibit suboptimal estimation performance in unsensed regions of the spatial domain. Moreover, the problem can become ill-posed in weakly observable systems (Cecilia and Costa-Castelló (2021)).

Closed-loop sensor placement methods directly address estimation error, disturbance rejection, and robustness by integrating sensor design with feedback design. Sun et al. (2019) combined POD and CFD data to optimize sensor locations for wind reconstruction, minimizing the estimation error under sensor noise. Kumar et al. (2014) optimized pressure and skin-friction sensors on a Coanda-jet airfoil using a POD-based flow reconstruction framework. Adjoint-based formulations have also been applied to PDE systems; for instance, Georges (2025) proposed a variational control approach for mobile actuator deployment in wildfire mitigation. Observer-based formulations, such as Burns and Herdman (2021), minimize the L^2 estimation error, offering a practical framework for observer-driven design. More recently, Seth et al. (2024) applied optimality criteria with orthogonal collocation using Lagrange polynomials to compensate for errors from reduced-order modeling. Collectively, these studies demonstrate the effectiveness of closed-loop formulations but also motivate further dedicated analysis of optimality in the infinite-dimensional setting.

In light of this discussion, the present work applies a quasi-steady adaptation of the General Pressure Equation (GPE) for pressure sensor placement analysis on rigid sails. A closed-loop sensor placement strategy is then formulated by combining pointwise pressure feedback with observer-based pressure reconstruction and embedding it within a finite-horizon optimization framework. The resulting formulation yields explicit local optimality conditions for specified sail configurations through an adjoint-based analysis conducted directly in the infinite-dimensional setting, avoiding reliance on reduced-order models. This approach provides a theoretical foundation for pressure-based sensing and feedback in rigid aerodynamic systems, representing a first step toward observer-driven sail control and CFD-informed experimental design.

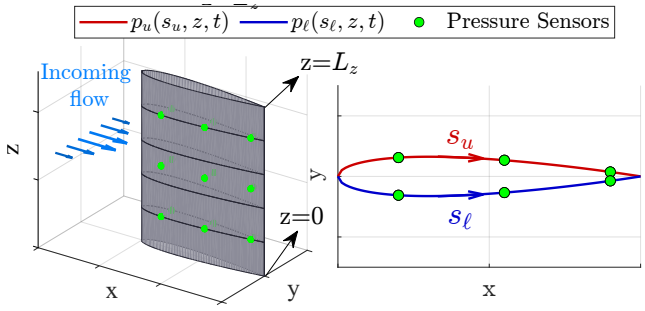

Fig. 1. Conceptual representation of the flow over a 3D rigid sail used for the pressure evolution modeling.

The paper is organized as follows: Section 2 outlines the pressure model, an observer that uses sparse measurements is provided in Section 3, and the optimal sensor placement problem is formulated and solved in Section 4. Sections 5 and 6 present simulation and experimental results, respectively.

2. PRESSURE FIELD MODELING

As the main motivation for automatic control of sails is to maximize the generated lift, the pressure distribution over the surface is of prime interest, and thus the focus of this section.

2.1 Pressure Evolution

The spatial coordinates are denoted as $\boldsymbol{\eta} = (s, z) \in \Omega$ and $\partial\Omega$ is the boundary of the domain of interest. The evolution of the thermodynamic pressure differential $p(\boldsymbol{\eta}, t) = p_u(s_u, z, t) - p_\ell(s_\ell, z, t)$ across a surface, such as the rigid sail shown in Fig. 1, is modeled using the GPE, derived from the compressible Navier–Stokes equations under low–Mach-number and isothermal flow assumptions (see Toutant (2017) for details). Close to quasi-steady base fields $\bar{p}(\boldsymbol{\eta})$ and $\bar{u}(\boldsymbol{\eta})$, representing steady aerodynamic loading at a fixed angle of attack (obtained from CFD simulations or experimental measurements), the linearized GPE gives the variation $\tilde{p}(\boldsymbol{\eta}, t) = p(\boldsymbol{\eta}, t) - \bar{p}(\boldsymbol{\eta})$ with dynamics

$$\begin{cases} \partial_t \tilde{p}(\boldsymbol{\eta}, t) = a_p(\partial_{ss}\tilde{p}(\boldsymbol{\eta}, t) + \partial_{zz}\tilde{p}(\boldsymbol{\eta}, t)) \\ \mathcal{G}\bar{H}(\boldsymbol{\eta}) = a_p(\partial_{ss}\bar{p}(\boldsymbol{\eta}) + \partial_{zz}\bar{p}(\boldsymbol{\eta}) + \bar{Q}(\boldsymbol{\eta})) \\ \tilde{p}(\boldsymbol{\eta}, 0) = 0, \quad \tilde{p}(\boldsymbol{\eta}, t)\big|_{\partial\Omega} = p(\boldsymbol{\eta}, t)\big|_{\partial\Omega} = 0. \end{cases} \tag{1}$$

The parameters in the non-dimensional form are defined as follows: $\mathcal{G} = \frac{\gamma}{\mathrm{Ma}^2}$ is the compressibility factor, where γ is the heat capacity ratio and Ma is the Mach number; $a_p = \frac{\gamma}{\mathrm{RePr}}$ is the pressure diffusivity, with Re and Pr denoting the Reynolds and Prandtl numbers, respectively. The surface normal velocity gradient is $\bar{H}(\boldsymbol{\eta}) = \partial_n \bar{u}(\boldsymbol{\eta})$, and $\bar{Q}(\boldsymbol{\eta}) = \partial_{nn}\bar{p}(\boldsymbol{\eta})$ represents the normal diffusive pressure gradient.

The pressure evolution model assumes weak wall-normal diffusion and perturbation velocity near the rigid boundary, i.e. $\partial_n \tilde{u}(\boldsymbol{\eta}, t) \approx \partial_{nn} \tilde{p}(\boldsymbol{\eta}, t) \approx 0$, consistent with boundary-layer scaling. The ratio of normal to tangential Strouhal numbers satisfies $St_n/St_s = \varepsilon/L \ll 1$, where ε is the boundary-layer thickness and L is the characteristic surface length. Since $\varepsilon \ll L$, then $|\partial_n \tilde{u}|/|\partial_s \tilde{u}| \gg 1$, and inertial effects are small ($St \ll 1$). Tangential convective and viscous terms are therefore neglected in (1), simplifying the model for sensor-placement analysis.

Remark 1. The GPE is formulated under a low Mach number assumption (Ma $\lesssim 0.1$), for which it accurately reproduces incompressible pressure dynamics while suppressing spurious acoustic effects (Toutant (2018)). The Reynolds number is a fixed, physical parameter of the system, while the Mach and Prandtl numbers are treated as numerical parameters controlling model behavior. Although extensions of the GPE include convective pressure transport terms to improve accuracy in strongly unsteady or turbulent regimes (Dupuy et al. (2020)), the present setting assumes attached flow, boundary-layer scaling, and quasi-steady operation. Under these conditions, tangential velocity gradients are negligible and the wall-normal velocity profile is effectively time-invariant, causing the convective contribution to collapse to a local reaction term that does not alter the spatial structure of the surface pressure.

Remark 2. The boundary conditions for $p(\boldsymbol{\eta}, t)$ at the spanwise edges $z = 0$ and $z = L_z$, taken along the s-direction are set to zero as a first-order approximation (see Fig. 1). This assumption reflects the presence of tip vortices, which induce a near-zero pressure difference at the sail boundaries.

2.2 Sensor Modeling

The two-dimensional spatial domain Ω associated with the rigid sail projection in Fig. 2 is partitioned into a set of subdomains defined as $\Omega_{ij} = [s_i, s_{i+1}] \times [z_j, z_{j+1}]$, where $i \in \mathcal{I} = \{1, \ldots, n\}$, and $j \in \mathcal{J} = \{1, \ldots, m\}$. The partitions along the s- and z-axes satisfy $0 = s_1 < s_2 < \cdots < s_{n+1} = L_s$ and $0 = z_1 < z_2 < \cdots < z_{m+1} = L_z$ such that the representative points are described on a shifted grid as $\bar{s}_i \in [s_i, s_{i+1}]$ and $\bar{z}_j \in [z_j, z_{j+1}]$.

Most sensors on a sail can only be placed at a finite number of discrete spatial locations. Accordingly, the sensing distribution is defined, for $i \in \mathcal{I}$, $j \in \mathcal{J}$, as

$$c_{ij}(\boldsymbol{\eta}) = \delta_D(\boldsymbol{\eta} - \bar{\boldsymbol{\eta}}_{ij}) = \delta_D(s - \bar{s}_i)\, \delta_D(z - \bar{z}_j), \quad (2)$$

where $\delta_D(\cdot)$ is the Dirac delta function. This form of $c_{ij}(\boldsymbol{\eta})$ represents pointwise sensing at discrete locations $\bar{\boldsymbol{\eta}}_{ij} = (\bar{s}_i, \bar{z}_j)$ within each subdomain $\Omega_{ij} \subset \Omega$. The measurement equation associated with the pressure evolution system (1) is defined as

$$\boldsymbol{y}(t) = \iint_{\Omega} \boldsymbol{c}(\boldsymbol{\eta})\, p(\boldsymbol{\eta}, t)\, d\boldsymbol{\eta} + \boldsymbol{g}(t), \quad (3)$$

where $\boldsymbol{y}(t) = [y_{11}(t), \ldots, y_{nm}(t)]^T$ denotes the measurement output vector, $\boldsymbol{c}(\boldsymbol{\eta}) = [c_{11}(\boldsymbol{\eta}), \ldots, c_{nm}(\boldsymbol{\eta})]^T$ is the stacked sensor kernel vector, and $\boldsymbol{g}(t)$ represents additive measurement disturbances accounting for sensor noise, bias, and modeling uncertainty.

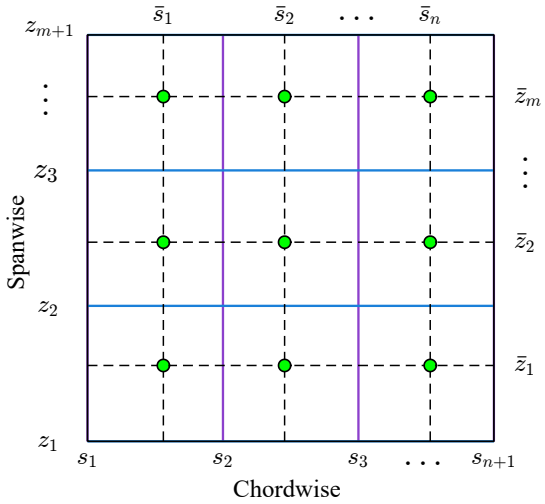

Fig. 2. Decomposition of the rigid sail surface into a 2D projected domain.

Since the Dirac delta function is inherently discontinuous and non-differentiable, a smooth approximation is employed to ensure differentiability of the observation operator, which is needed for gradient-based optimization. Using a Gaussian kernel with variance parameters σ_s^2 and σ_z^2, the regularized sensing function is expressed as

$$\begin{cases} \delta_D(\boldsymbol{\eta} - \bar{\boldsymbol{\eta}}_{ij}) \simeq \dfrac{1}{\Gamma(\bar{\boldsymbol{\eta}}_i)} f(\boldsymbol{\eta}; \bar{\boldsymbol{\eta}}_{ij}) \\ f(\boldsymbol{\eta}; \bar{\boldsymbol{\eta}}_{ij}) = \exp\Big(- \Big[\dfrac{(s - \bar{s}_i)^2}{\sigma_s^2} + \dfrac{(z - \bar{z}_j)^2}{\sigma_z^2} \Big] \Big) \\ \Gamma(\bar{\boldsymbol{\eta}}_{ij}) = \displaystyle\iint_{\Omega} f(\boldsymbol{\eta}; \bar{\boldsymbol{\eta}}_{ij})\, d\boldsymbol{\eta}. \end{cases} \quad (4)$$

Consequently, the spatial gradient of the sensing kernel with respect to the sensor location $\bar{s}_i$ is given by

$$\begin{cases} \partial_{\bar{s}_i} \delta_D(\boldsymbol{\eta} - \bar{\boldsymbol{\eta}}_{ij}) \simeq \delta_D(\cdot) \left[\dfrac{2(s - \bar{s}_i)}{\sigma_s^2} - \dfrac{1}{\Gamma(\bar{\boldsymbol{\eta}}_{ij})} \partial_{\bar{s}_i} \Gamma(\bar{\boldsymbol{\eta}}_{ij}) \right], \\ \partial_{\bar{s}_i} \Gamma(\bar{\boldsymbol{\eta}}_i) = \displaystyle\iint_{\Omega} \left(\dfrac{2(s - \bar{s}_i)}{\sigma_s^2} \right) f(\boldsymbol{\eta}; \bar{\boldsymbol{\eta}}_{ij})\, d\boldsymbol{\eta}. \end{cases} \quad (5)$$

The approximated gradient with respect to $\bar{z}_j$ is defined analogously.

Remark 3. The kernel is normalized so that $\iint_{\Omega} \delta_D(\boldsymbol{\eta} - \bar{\boldsymbol{\eta}}_{ij})\, d\boldsymbol{\eta} = 1$, ensuring conservation of the reconstructed measurement. The center $(\bar{s}_i, \bar{z}_j)$ denotes the sensor location, while the variance σ controls the effective sensing region. Smaller σ yields sharper, more localized measurements but may induce steep gradients, whereas larger σ smooths the response over a wider area at the expense of bias. During the optimal design procedure, σ is selected relative to the spatial scale to balance exact measurement and information propagation.

3. POINTWISE LUENBERGER OBSERVER DESIGN

Based on the linear system dynamics structure (1), we consider the observer of the following structure

$$\begin{cases} \partial_t \hat{\tilde{p}}(\boldsymbol{\eta},t) = a_p\big(\partial_{ss}\hat{\tilde{p}}(\boldsymbol{\eta},t) + \partial_{zz}\hat{\tilde{p}}(\boldsymbol{\eta},t)\big) - W(\boldsymbol{\eta}) \\ \qquad\qquad + \boldsymbol{c}^T(\boldsymbol{\eta})\boldsymbol{K}(\boldsymbol{y}(\boldsymbol{\eta},t) - \hat{\boldsymbol{y}}(\boldsymbol{\eta},t)), \\ \mathcal{G}\bar{H}_N(\boldsymbol{\eta}) = a_p(\partial_{ss}\hat{\bar{p}}(\boldsymbol{\eta}) + \partial_{zz}\hat{\bar{p}}(\boldsymbol{\eta}) + \bar{Q}_N(\boldsymbol{\eta})) \\ \quad W(\boldsymbol{\eta}) = \mathcal{G}(\bar{H}(\boldsymbol{\eta}) - \bar{H}_N(\boldsymbol{\eta})) \\ \qquad\qquad - a_p(\bar{Q}(\boldsymbol{\eta}) - \bar{Q}_N(\boldsymbol{\eta})) \\ \quad \hat{p}(\boldsymbol{\eta},t) = \hat{\bar{p}}(\boldsymbol{\eta}) + \hat{\tilde{p}}(\boldsymbol{\eta},t) \\ \quad \hat{p}(\boldsymbol{\eta},0) = \hat{\bar{p}}(\boldsymbol{\eta}), \;\; \hat{\tilde{p}}(\boldsymbol{\eta},t)\big|_{\partial\Omega} = \hat{p}(\boldsymbol{\eta},t)\big|_{\partial\Omega} = 0, \end{cases} \tag{6}$$

where $\hat{\tilde{p}}(\boldsymbol{\eta},t)$ denotes the estimated pressure perturbation, $\hat{\bar{p}}(\boldsymbol{\eta})$ is the quasi-steady base pressure field obtained by solving Poisson's equation for a given pair of distributions $\bar{H}_N(\boldsymbol{\eta})$ and $\bar{Q}_N(\boldsymbol{\eta})$. The correction term $W(\boldsymbol{\eta})$ accounts for discrepancies between the system and observer base fields, ensuring $L^2(\Omega)$ convergence.

The convergence of the observer is analyzed using the estimation error between the system and observer, defined as $e(\boldsymbol{\eta},t) = p(\boldsymbol{\eta},t) - \hat{p}(\boldsymbol{\eta},t)$. Combining (1) and (6) yields the following error dynamics

$$\begin{cases} \partial_t e(\boldsymbol{\eta},t) = a_p\big(\partial_{ss}e(\boldsymbol{\eta},t) + \partial_{zz}e(\boldsymbol{\eta},t)\big) + \boldsymbol{d}(\boldsymbol{\eta},t) \\ \qquad\qquad - \boldsymbol{c}^T(\boldsymbol{\eta})\boldsymbol{K}\iint_\Omega \boldsymbol{c}(\boldsymbol{\eta})e(\boldsymbol{\eta},t)\,d\boldsymbol{\eta}, \\ \mathcal{G}(\bar{H}(\boldsymbol{\eta}) - \bar{H}_N(\boldsymbol{\eta})) = a_p\Big(\partial_{ss}\bar{e}(\boldsymbol{\eta}) + \partial_{zz}\bar{e}(\boldsymbol{\eta}) \\ \qquad\qquad + (\bar{Q}(\boldsymbol{\eta}) - \bar{Q}_N(\boldsymbol{\eta}))\Big) \\ e(\boldsymbol{\eta},0) = \bar{e}(\boldsymbol{\eta}), \;\; e(\boldsymbol{\eta},t)\big|_{\partial\Omega} = 0, \end{cases} \tag{7}$$

where $\bar{e}(\boldsymbol{\eta}) = \bar{p}(\boldsymbol{\eta}) - \hat{\bar{p}}(\boldsymbol{\eta})$ denotes the steady state error between the system and observer base fields. This term appears because the system and observer may be linearized around different environmental conditions (distinct $\bar{H}(\boldsymbol{\eta})$ and $\bar{Q}(\boldsymbol{\eta})$ distributions), such as wind speeds and angle of attack. The term $\boldsymbol{d}(\boldsymbol{\eta},t) = -\boldsymbol{c}^T(\boldsymbol{\eta})\boldsymbol{K}\boldsymbol{g}(t)$ represents an additive disturbance due to sensor uncertainty and noise. The convergence of the observer is obtained from the following Theorem (proof in Appendix A).

Theorem 1. Consider the linear estimation error dynamics (7), where $e(\boldsymbol{\eta},t) \in C^1([0,\infty); L^2(\Omega))$ and with pointwise-in-space measurements given by (3). Assume that the measurement disturbance is bounded and that there exists a constant κ satisfying $\kappa \in (0,2)$. If there exists scalars $\beta_0 > 0$ and $\bar{k}_{ij},\ i \in \mathcal{I},\ j \in \mathcal{J}$ satisfying the linear matrix inequality (LMI):

$$\boldsymbol{\Psi}_{ij} \triangleq \begin{bmatrix} -\vartheta\left(\frac{1}{\phi_i} + \frac{1}{\varphi_j}\right) & \frac{\vartheta}{\phi_i} & \frac{\vartheta}{\varphi_j} & 0 \\ \frac{\vartheta}{\phi_i} & -\frac{\vartheta}{\phi_i} & 0 & 0 \\ \frac{\vartheta}{\varphi_j} & 0 & -\frac{\vartheta}{\varphi_j} & 0 \\ 0 & 0 & 0 & -\frac{\bar{k}_{ij}\left(1-\frac{\kappa}{2}\right)}{A_{ij}} \end{bmatrix} < 0, \tag{8}$$

with $\phi_i = \max\{(\bar{s}_i - s_i)^2, (s_{i+1} - \bar{s}_i)^2\}$, $\varphi_j = \max\{(\bar{z}_j - z_j)^2, (z_{j+1} - \bar{z}_j)^2\}$, $k_{ij} = \frac{\bar{k}_{ij}}{\beta_0}$, $\vartheta = \frac{a_p\beta_0\pi^2}{4}$, and $A_{ij} = (s_{i+1} - s_i)(z_{j+1} - z_j)$, then there exists a constant $0 < \varrho < \min\{\varrho_{ij}^{\max}\}$, with

$$\varrho_{ij}^{\max} = 2\,\min\Big\{\vartheta\Big(\tfrac{1}{\phi_i} + \tfrac{1}{\varphi_j} - \sqrt{(\tfrac{1}{\phi_i})^2 - \tfrac{1}{\phi_i\varphi_j} + (\tfrac{1}{\varphi_j})^2}\Big), \tfrac{\bar{k}_{ij}(1-\frac{\kappa}{2})}{A_{ij}}\Big\}, \tag{9}$$

such that the estimation error satisfies

$$\lim_{t\to\infty} \|e(\cdot,t)\|_{L^2(\Omega)} \le \sqrt{\frac{2C_g}{\varrho}}. \tag{10}$$

Here, $C_g = \sum_{i=1}^n \sum_{j=1}^m \frac{\bar{k}_{ij}}{2\kappa} g_{\max}^2$ where $g_{\max}$ is the bound on the measurement disturbance defined in (A.3). The system (7) is thus exponentially stable with an ultimate bound in the $L^2(\Omega)$ sense, and (6) provides a suitable state observer for the linearized GPE in (1).

4. OPTIMAL SENSOR PLACEMENT DESIGN FOR PRESSURE OBSERVATIONS

In this setting, the optimal sensor placement problem is formulated by defining a quantitative measure of the estimation error to be minimized over a finite time horizon $t \in [0, T_f]$ for a scenario of specific interest. Given an initial error field $\bar{e}(\boldsymbol{\eta})$, one may consider minimizing this error over a finite interval when accurate state reconstruction is crucial. From the perspective of automatic sail control, a tacking maneuver, which is a heading change into the wind, is considered in representative wind conditions as a transient operating regime where improvements in sail efficiency are most impactful. This naturally leads to the following optimal sensor placement problem as

$$\min_{\bar{s}_i,\,\bar{z}_j} \;\; J(e,\bar{s}_i,\bar{z}_j) = \frac{q_1}{2}\int_0^{T_f}\iint_\Omega e^2(\boldsymbol{\eta},t)\,d\boldsymbol{\eta}\,dt + \frac{q_2}{2}\sum_{i=1}^n\sum_{j=1}^m \|\bar{\boldsymbol{\eta}}_{ij} - \bar{\boldsymbol{\eta}}_{ij}^d\|_2^2, \tag{11}$$

$$\text{s.t.} \quad e(\cdot,t) \text{ obeys the error dynamics (7)}, \tag{12}$$

$$(\bar{s}_i,\bar{z}_j) \in \Omega_{ij} \subset \Omega, \quad i \in \mathcal{I},\ j \in \mathcal{J}, \tag{13}$$

where $\bar{\boldsymbol{\eta}}_{ij}^d = (\bar{s}_i^d, \bar{z}_j^d)$ denotes a nominal (preferred) sensor location, and $q_1, q_2 \ge 0$ are scalar weighting coefficients. To balance the relative magnitude of the error-integral term and the design-deviation term without altering the adjoint dynamics, the weight q_2 can be parameterized as

$$q_2 = \tilde{q}_2\frac{E_0}{D_{ij}^2},$$

where $E_0 = \int_0^{T_f}\iint_\Omega e^2(\boldsymbol{\eta},t)\,d\boldsymbol{\eta}\,dt$ is the initial time-integrated estimation error and $D_{ij} = \max_{\boldsymbol{\eta}\in\partial\Omega_{ij}} \|\boldsymbol{\eta} - \bar{\boldsymbol{\eta}}_{ij}^d\|_2$ denotes the maximum admissible displacement within Ω_{ij}. The relative magnitudes of q_1 and $\tilde{q}_2$ tune the contribution of each term, and both are kept (instead of just their ratio) for numerical conditioning purposes.

To characterize necessary conditions for an extremum, the Lagrangian approach is used by introducing the adjoint state $\lambda(\boldsymbol{\eta},t) \in C^1([0,T_f]; L^2(\Omega))$ associated with the error dynamics in Eq. (7). The Lagrangian function is then constructed by combining the cost functional in Eq. (11) with the constraint imposed by the error dynamics, giving

$$\begin{aligned} \mathcal{L} = {} & \frac{q_1}{2}\int_0^{T_f}\iint_\Omega e^2(\boldsymbol{\eta},t)\,d\boldsymbol{\eta}\,dt + \frac{q_2}{2}\sum_{i=1}^n\sum_{j=1}^m \|\bar{\boldsymbol{\eta}}_{ij} - \bar{\boldsymbol{\eta}}_{ij}^d\|_2^2 \\ & + \int_0^{T_f}\iint_\Omega \lambda(\boldsymbol{\eta},t)\Big[\partial_t e(\boldsymbol{\eta},t) - a_p\partial_{\boldsymbol{\eta}\boldsymbol{\eta}}e(\boldsymbol{\eta},t) \\ & + \boldsymbol{c}^T(\boldsymbol{\eta})\boldsymbol{K}\iint_\Omega \boldsymbol{c}(\boldsymbol{\xi})e(\boldsymbol{\xi},t)\,d\boldsymbol{\xi}\Big]\,d\boldsymbol{\eta}\,dt, \end{aligned} \tag{14}$$

where $\partial_{\boldsymbol{\eta}\boldsymbol{\eta}} = \partial_{ss} + \partial_{zz}$ and $\boldsymbol{\xi} = (s, z) \in \Omega$. The first-order necessary conditions for optimality are obtained by computing the Gâteaux derivative of $\mathcal{L}$ with respect to $e(\boldsymbol{\eta}, t)$ and to the sensor locations $(\bar{s}_i, \bar{z}_j)$.

Theorem 2. Let $e(\boldsymbol{\eta}, t)$ evolve according to (7) for $t \in [0, T_f]$. Let the sensing kernels $c_{ij}(\boldsymbol{\eta})$ depend smoothly on the sensor coordinates $(\bar{s}_i, \bar{z}_j)$, and consider the optimization problem (11). Then, the first-order necessary conditions for an optimum are obtained if there exists a unique weak adjoint state $\lambda(\boldsymbol{\eta}, t) \in C^1([0, T_f]; L^2(\Omega))$ satisfying

$$
\begin{aligned}
&q_1 e(\boldsymbol{\eta}, t) - \partial_t \lambda(\boldsymbol{\eta}, t) - a_p \partial_{\boldsymbol{\eta}\boldsymbol{\eta}} \lambda(\boldsymbol{\eta}, t) \\
&\quad + \boldsymbol{c}^T(\boldsymbol{\eta}) \boldsymbol{K} \iint_\Omega \boldsymbol{c}(\boldsymbol{\xi}) \lambda(\boldsymbol{\xi}, t)\, d\boldsymbol{\xi} = 0, \ \forall \boldsymbol{\eta}, \forall \boldsymbol{\xi} \in \Omega, \quad (15) \\
&\lambda(\boldsymbol{\eta}, T_f) = 0, \ \lambda(\boldsymbol{\eta}, t)\big|_{\partial\Omega} = 0, \ \forall t \in [0, T_f],
\end{aligned}
$$

and if the sensor positions $(\bar{s}_i, \bar{z}_j)$ for $i \in \mathcal{I}$ and $j \in \mathcal{J}$ are such that, $\forall \boldsymbol{\eta}, \forall \boldsymbol{\xi} \in \Omega$,

$$
\begin{aligned}
\partial_{\bar{s}_i} j(\bar{\boldsymbol{\eta}}_{ij}) \doteq k_{ij} \int_0^{T_f} \iint_\Omega e(\boldsymbol{\eta}, t) \Big[\partial_{\bar{s}_i} c_{ij}(\boldsymbol{\eta}) \iint_\Omega c_{ij}(\boldsymbol{\xi}) \lambda(\boldsymbol{\xi}, t)\, d\boldsymbol{\xi} \\
+ c_{ij}(\boldsymbol{\eta}) \iint_\Omega \partial_{\bar{s}_i} c_{ij}(\boldsymbol{\xi}) \lambda(\boldsymbol{\xi}, t)\, d\boldsymbol{\xi} \Big] d\boldsymbol{\eta}\, dt \\
+ q_2(\bar{s}_i - s_{d,i}) = 0, \quad (16)
\end{aligned}
$$

$$
\begin{aligned}
\partial_{\bar{z}_j} j(\bar{\boldsymbol{\eta}}_{ij}) \doteq k_{ij} \int_0^{T_f} \iint_\Omega e(\boldsymbol{\eta}, t) \Big[\partial_{\bar{z}_j} c_{ij}(\boldsymbol{\eta}) \iint_\Omega c_{ij}(\boldsymbol{\xi}) \lambda(\boldsymbol{\xi}, t)\, d\boldsymbol{\xi} \\
+ c_{ij}(\boldsymbol{\eta}) \iint_\Omega \partial_{\bar{z}_j} c_{ij}(\boldsymbol{\xi}) \lambda(\boldsymbol{\xi}, t)\, d\boldsymbol{\xi} \Big] d\boldsymbol{\eta}\, dt \\
+ q_2(\bar{z}_j - z_{d,j}) = 0. \quad (17)
\end{aligned}
$$

where $\partial_{\bar{s}_i} j(\bar{\boldsymbol{\eta}}_{ij})$ and $\partial_{\bar{z}_j} j(\bar{\boldsymbol{\eta}}_{ij})$ denote the gradients of the reduced cost functional with respect to the sensor coordinates (used in the following for numerical resolution).

The proof for Theorem 2 can be found in Appendix B.

Equations (7) and (15)-(17) together form a two-point boundary value problem (BVP) in space and time. If an optimal sensor configuration $(\bar{s}_i, \bar{z}_j)$ exists $\forall t \in [0, T_f]$, it must satisfy this BVP. In this work, a Newton-type interior-point method (Byrd et al. (1999)) is used to iteratively minimize the reduced cost functional under the prescribed constraints (7), (15) and gradients $\partial_{\bar{s}_i} j(\bar{\boldsymbol{\eta}}_{ij})$ and $\partial_{\bar{z}_j} j(\bar{\boldsymbol{\eta}}_{ij})$, providing a numerical solution to the two-point BVP. The solver is implemented given the pressure diffusivity a_p, the gradient design distributions $\bar{H}(\boldsymbol{\eta}), \bar{H}_N(\boldsymbol{\eta})$ and $\bar{Q}(\boldsymbol{\eta}), \bar{Q}_N(\boldsymbol{\eta})$, and an initial sensor configuration. The iterative procedure to solve the optimal design problem (11) under constraints (13) is as follows:

(1) for a given sensor configuration $(\bar{s}_i, \bar{z}_j)$ and a selected robustness constant $\kappa \in (0, 2)$, solve the LMIs (8) to determine stabilizing observer gains k_{ij} at the current optimization step;
(2) numerically solve systems (1) and (6) over the time domain of interest $t \in [0, T_f]$ for the current sensor configuration;
(3) given $e(\boldsymbol{\eta}, t)$ for $t \in [0, T_f]$, solve the adjoint system (15) backwards in time to obtain the Lagrange multiplier distribution $\lambda(\boldsymbol{\eta}, t)$;
(4) evaluate the gradients $\partial_{\bar{s}_i} j(\bar{\boldsymbol{\eta}}_{ij})$ and $\partial_{\bar{z}_i} j(\bar{\boldsymbol{\eta}}_{ij})$, according to (16) and (17) to provide the interior-point solver with a descent direction for updating the sensors positions.

Remark 4. In simulations, the nominal sensor locations $\bar{\boldsymbol{\eta}}_{ij}^d$ can be chosen as the geometric centers of their admissible subdomains Ω_{ij}. This choice provides a uniformly distributed baseline configuration that ensures spatial coverage of the domain while avoiding clustering, and serves as a neutral reference around which the optimizer refines the sensor locations. In practical deployments, $\bar{\boldsymbol{\eta}}_{ij}^d$ can incorporate additional engineering constraints, such as proximity to power or communication infrastructure, wiring length, accessibility, or structural mounting limitations. The regularization constraint involving $\bar{\boldsymbol{\eta}}_{ij}^d$ thus provides a method to consider deployment preferences.

Remark 5. At each iteration, the observer gains are determined independently by solving an LMI feasibility problem that minimizes the gain magnitude while ensuring the stability of the estimation dynamics. The LMI condition, denoted by $\boldsymbol{\Psi}_{ij} < 0$, is therefore not included explicitly in (11). Instead, we assume the existence of feasible gains for all admissible sensor configurations, which is guaranteed under mild geometric and positivity conditions.

5. SIMULATION EXAMPLE

Consider the state and observer systems (1) and (6), with physical parameters chosen as in Table 1. The system and observer linearizations are initialized with gradient distributions $\bar{H}(\boldsymbol{\eta}), \bar{H}_N(\boldsymbol{\eta})$ and $\bar{Q}(\boldsymbol{\eta}), \bar{Q}_N(\boldsymbol{\eta})$, designed to emphasize normal gradients at the leading edge for the system and the trailing edge for the observer. The quasi-steady distributions $\bar{p}(\boldsymbol{\eta})$ and $\hat{\bar{p}}(\boldsymbol{\eta})$ are obtained by numerically solving the corresponding Poisson equations over Ω. These distributions are illustrated in Fig. 3, and the resulting initial observer error $\bar{e}(\boldsymbol{\eta})$ is shown in Fig. 4. The projection of the rigid sail is defined over the domain $\Omega = [0, L_s] \times [0, L_z]$, with $L_s = L_z = 1$. The domain is discretized into subdomains $\Omega_{ij} = [s_i, s_{i+1}] \times [z_j, z_{j+1}]$, where s_{ij} and z_{ij} are listed in Table 1. These values are chosen to give each sensor sufficient coverage while avoiding target sensor locations on the boundaries Four sensor configurations $\boldsymbol{\Xi}_q$, $q \in \{1, 2, 3, \text{opt}\}$ are described in Table 2 and presented in Fig. 4. The nominal sensor locations $\bar{\boldsymbol{\eta}}_{ij}^d$ are selected at the center of each subdomain. The initial sensor locations for the optimization algorithm are selected near the center (see Fig. 5(b)) which serves only as a feasible initialization.

The forward error system (7) is integrated over $t \in [0, T_f]$ using an explicit Euler finite-difference scheme. Similarly, the adjoint system (15) is solved backward in time. A uniform observer gain k_{ij} (see Table 1) yields stable conver-

Table 1. System and optimization parameters used in simulation and experiment.

Simulations
$\text{Re} = 2 \times 10^5$, $\text{Ma} = 0.02$, $\gamma = 1.4$, $\text{Pr} = 0.71$
$a_p = 9.86 \times 10^{-6}$, $\mathcal{G} = 3.5 \times 10^3$, $\sigma_s = \sigma_z = 0.1$
$\kappa = 0.5$, $k_{ij} = 0.323$, $q_1 = 1.8$, $\tilde{q}_2 = 0.5$
$ds = dz = 0.01$, $dt = 0.1$ s, $T_f = 1000$ s
$s_1 = 0, s_2 = 0.4, s_3 = L_s$; $z_1 = 0, z_2 = 0.5, z_3 = L_z$
Experimental Implementation
$a_p = 2.91 \times 10^{-5}$ m^2/s, $\mathcal{G} = 1.41 \times 10^5$ Pa, $\sigma_s = \sigma_z = 0.1$
$\kappa = 0.5$, $k_{ij} = 0.335$, $q_1 = 1$, $\tilde{q}_2 = 0$
$ds = dz = 0.01$, $dt = 0.1$ s, $T_f = 500$ s
$s_1 = 0, s_2 = 0.28, s_3 = L_s$; $z_1 = 0, z_2 = 0.33, z_3 = 0.66, z_4 = L_z$

Table 2. Sensor placement configurations Ξ_q.

	Ω_{11}	Ω_{12}	Ω_{21}	Ω_{22}
Ξ_1	(0.2, 0.25)	(0.2, 0.75)	(0.7, 0.25)	(0.7, 0.75)
Ξ_2	(0.35, 0.05)	(0.35, 0.9)	(0.5, 0.05)	(0.85, 0.9)
Ξ_3	(0.18, 0.48)	(0.18, 0.52)	(0.81, 0.43)	(0.81, 0.52)
Ξ_{opt}	(0.19, 0.41)	(0.25, 0.62)	(0.82, 0.31)	(0.81, 0.65)

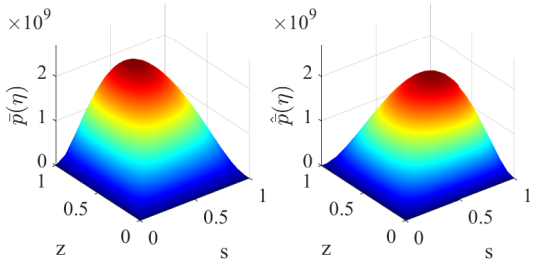

Fig. 3. Linearized base distributions for the system $\bar{p}(\boldsymbol{\eta})$ and the observer $\hat{\bar{p}}(\boldsymbol{\eta})$.

gence for all configurations. Gradients of the reduced cost functional with respect to the sensor positions, $\partial_{\bar{s}_i} j(\bar{\boldsymbol{\eta}}_{ij})$ and $\partial_{\bar{z}_j} j(\bar{\boldsymbol{\eta}}_{ij})$, are numerically computed.

All relevant numerical parameters, including discretization (ds, dz, dt), optimization horizon T_f, and weighting coefficients, are listed in Table 1. To maintain numerical robustness and tractable optimization times, the cost functional is evaluated over a truncated horizon, which captures the dominant transient characteristics of the error dynamics. The sensor configuration Ξ_{opt} is obtained via interior-point optimization using MATLAB's `fmincon` solver, with internal problem scaling enabled to improve conditioning. On a standard workstation, a single optimization requires approximately 40 s per solver iteration. The optimization terminates when a step tolerance of 10^{-3} is satisfied, and the optimization evolution is presented in Fig. 5.

The weights q_1 and $\tilde{q}_2$ (Table 1) are chosen such that the error-integral term dominates the cost functional, while increasing $\tilde{q}_2$ tends to bring the solution closer to $\bar{\boldsymbol{\eta}}^d_{ij}$.

The following measurement operator

$$\mathcal{C}_{\Xi_q} : p(\boldsymbol{\eta}, t) \mapsto [p(\bar{\boldsymbol{\eta}}_{11}, t), \ldots, p(\bar{\boldsymbol{\eta}}_{nm}, t)], \; q \in \{1, 2, 3, \text{opt}\},$$

is used for sensor performance analysis. In Fig. 6, the normalized $L^2(\Omega)$ convergence of the observer error is presented for all sensor configurations Ξ_q. Among these, Ξ_2 exhibits the slowest convergence because its sensors sample regions where the system–observer error is small and its gradients are weak. As a result, the projected error signal $\mathcal{C}_{\Xi_2} e(\boldsymbol{\eta}, t)$ carries little information about the true error field, limiting corrective error feedback in the observer.

In contrast, Ξ_3 places sensors in areas of steep error gradients but clusters them within a region smaller than the characteristic length scale of $e(\boldsymbol{\eta}, t)$. This spatial redundancy lowers the rank of $\mathcal{C}_{\Xi_3}$, as multiple sensors capture similar dynamics and reduce independent information. The central configuration Ξ_1 achieves a balanced compromise, distributing sensors across zones of moderate error and velocity gradients while maintaining adequate spacing. The optimized configuration Ξ_{opt}, obtained via the proposed gradient-based algorithm, places sensors in

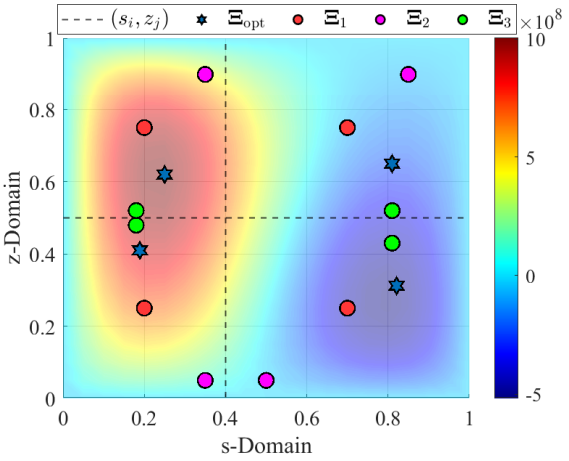

Fig. 4. Sensor placements over the initial observer system error distribution $\bar{e}(\boldsymbol{\eta})$.

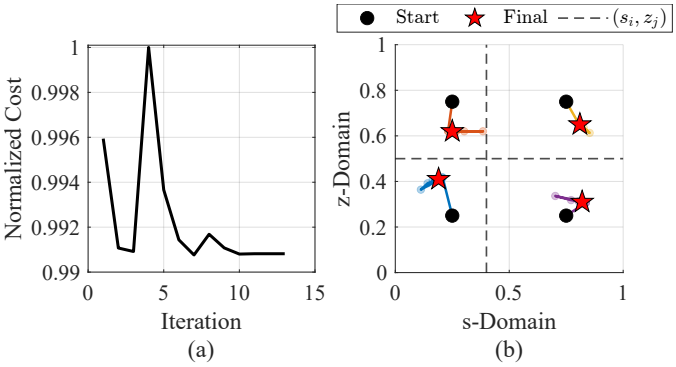

Fig. 5. Optimization evolution profiles (simulation): (a) Cost profile evolution; (b) Sensor placement evolution.

regions of large state and error gradients while maintaining spatial decorrelation. This maximizes independent measurement information and accelerates convergence of $\|e(\boldsymbol{\eta}, t)\|_{L^2(\Omega)} \to 0$.

Measurement uncertainty is represented by $g(t)$ as additive sensor noise and slowly varying bias with prescribed variance and correlation time. Since this noise is independent of sensor location and enters the observer dynamics uniformly, its contribution to the time-integrated $L^2(\Omega)$ estimation error is negligible compared to the deterministic error dynamics and does not affect optimal sensor placement. By contrast, flow-induced pressure fluctuations from turbulent or shear-dominated conditions are spatially dependent and vary with local velocity or pressure gradients. Accounting for these effects would couple measurement noise with sensor location, potentially altering optimal sensor placement.

Remark 6. Owing to the modeling assumptions in Section 2.1, the linearized pressure observer behaves as a weakly diffusive system, with diffusion diminishing as the Reynolds number increases. In the low–Mach-number limit, the observer convergence is primarily influenced by the velocity gradient terms $\bar{H}(\boldsymbol{\eta}), \bar{H}_N(\boldsymbol{\eta})$ within $W(\boldsymbol{\eta})$, which reflects the inertial coupling in the steady dynamics. Despite this simplification, the formulation offers a useful first-order approximation for the optimal sensor

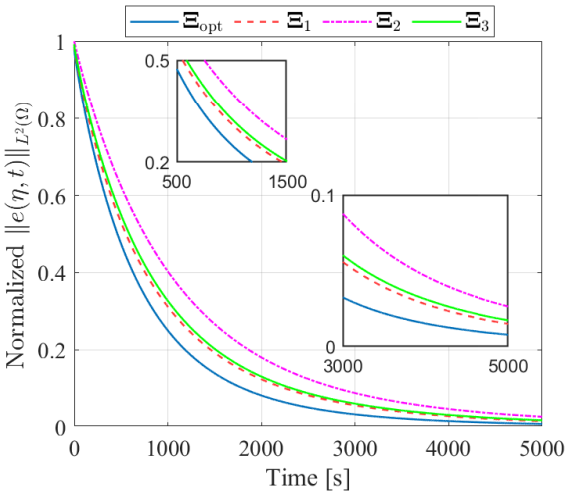

Fig. 6. The normalized $\|e(\boldsymbol{\eta}, t)\|_{L^2(\Omega)}$ convergence for each sensor configuration.

placement, capturing the relative sensitivity of each sensor location on the surface.

6. EXPERIMENTAL RESULTS

The experimental setup, shown in Fig. 7, consists of pressure probes mounted on the jib sail of a Mouette 19 sailboat (5.94 m fractional sloop dinghy built by Paceship Yachts Ltd in 1974). Four probes on each side are positioned directly opposite one another and measure pointwise pressure differentials at the optimized locations. Each probe is connected via tubing to Honeywell differential pressure sensors integrated on a custom I2C board with a Raspberry Pi Pico for data logging. Wind speed and direction are measured using a Calypso Ultrasonic Portable Mini Anemometer. An onboard computer communicates with the Pico and anemometer and stores all the data.

Each differential pressure sensor was connected at one port to a 3D-printed flow probe mounted on the sail surface, while the second port was connected to a common 3D-printed storage hub. The hub is assumed to maintain a spatially uniform reference pressure, such that the measured differential pressure reflects local surface pressure variations relative to this reference. All sensors were configured identically, ensuring consistency across measurement locations. Prior to data collection, sensors were verified to exhibit near-zero differential output under no-flow conditions, confirming consistent baseline behavior across channels. To reduce high-frequency sensor noise and small-scale flow fluctuations, the pressure signals were low-pass filtered during post-processing. While the manufacturer-specified Total Error Band (±1.5% of full-scale) provides a conservative bound on absolute measurement uncertainty, this uncertainty does not influence the sensor placement results, as the optimization is driven by time-integrated spatial error dynamics rather than instantaneous measurement noise.

The real sail is approximated as a rigid surface consistent with the modeling proposed in Section 2.1. If additional effects such as sail twist or mast interference were incorporated into the design model, they would enter through modified quasi-steady pressure distributions

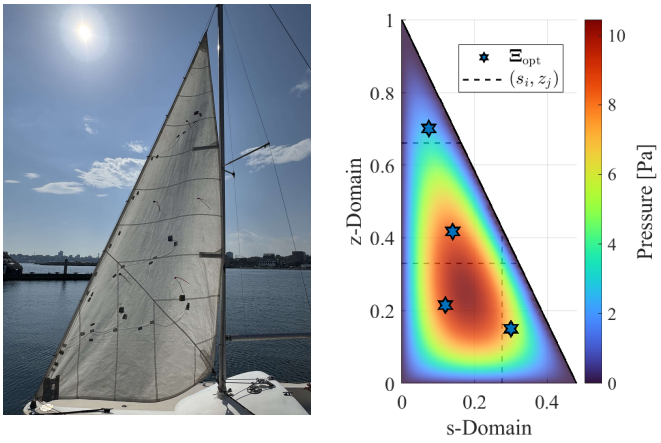

Fig. 7. Experimental hardware setup on a 6 m sailboat from Dalhousie University and the corresponding optimal pressure sensor configuration on the sail, shown over the initial error distribution $\bar{e}(\boldsymbol{\eta})$.

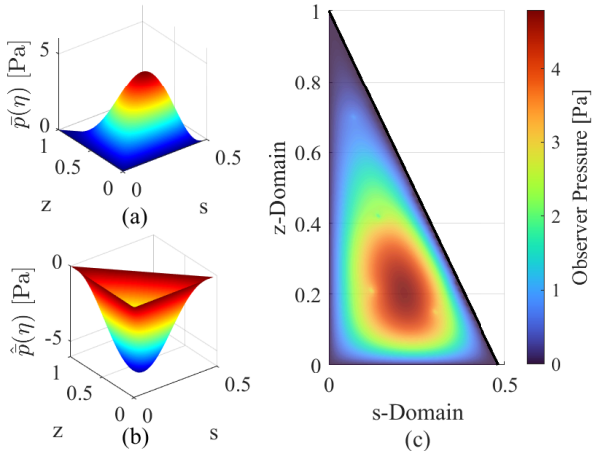

Fig. 8. Pressure profiles: (a) quasi-steady system pressure distribution; (b) quasi-steady observer pressure distribution; (c) observer pressure field with hardware sensor feedback.

and could lead to different optimal sensor configurations. However, such effects are not considered in the present offline optimization framework. The quasi-steady pressure distributions $\bar{p}(\boldsymbol{\eta})$ and $\hat{\bar{p}}(\boldsymbol{\eta})$ are obtained using the Poisson formulation (illustrated in Fig. 8(a)–(b)) with dimensional system parameters listed in Table 1. These distributions are generated based on gradient fields $\bar{H}(\boldsymbol{\eta}), \bar{H}_N(\boldsymbol{\eta})$ and $\bar{Q}(\boldsymbol{\eta}), \bar{Q}_N(\boldsymbol{\eta})$ that simulated a left-to-right wind, producing higher pressures on the windward side. The magnitudes are scaled such that the resulting pressure fields are consistent with the measured data. The measured sail geometry is mapped to a normalized computational domain (see Fig. 7). Sensor locations are optimized over prescribed subdomains Ω_{ij}, which are listed in Table 1. The optimization uses the same spatial discretization and timestep as Section 5 and is evaluated over a horizon of $T_f = 500\,\text{s}$, where the optimization evolution is presented in Fig. 9. The weights q_1 and $\tilde{q}_2$ (Table 1) are chosen such that only the error-integral term contributes to the cost function.

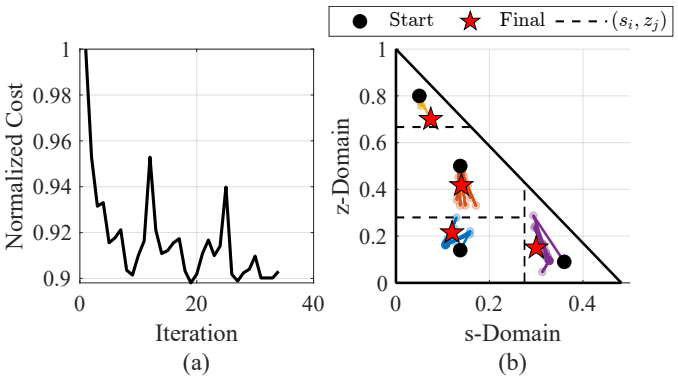

Fig. 9. Optimization evolution profiles (experiment): (a) Cost profile evolution; (b) Sensor placement evolution.

Using the measured wind direction (approximately 240°) and pressure feedback, the observer (6) is simulated for steady wind speeds of 2–4 m/s. The convergence results are shown in Fig. 8(c). While local corrections align closely with hardware measurements, global adjustments across the pressure field remain small due to weak diffusion effects.

7. CONCLUSION

This work proposes a theoretical framework for the optimal placement of pressure sensors on rigid sails, with a design based on a linearized pressure evolution model under quasi-steady flow conditions. The performance criterion measures the integrated observation error for a given maneuver. By combining an observer formulation with adjoint-based optimization, local optimality conditions are derived explicitly in the infinite-dimensional setting, enabling a gradient-based search for optimal sensor configurations. A numerical example illustrates that the method effectively identifies sensor locations in regions of high pressure variability while preserving spatial representativeness across the domain. Experimental results are obtained on a real-world 6 m sailboat sail.

Ongoing research focuses on developing multi-observer schemes capable of operating under varying aerodynamic conditions through adaptive parameter estimation and time-varying Gaussian fusion. These extensions aim to advance the current observer framework toward real-time pressure estimation and, ultimately, feedback control of rigid sails governed by nonlinear Navier–Stokes pressure dynamics. Finally, while measurement noise is modeled independently of sensor location, flow-induced pressure fluctuations could couple noise with location, potentially affecting optimal sensor placement; developing such noise models is left for future work.

REFERENCES

Armaou, A. and Demetriou, M.A. (2014). Optimal sensor placement and scheduling of hybrid PDEs arising in environmental and meteorological applications. In *Proc. of the 21st International Symposium on Mathematical Theory of Networks and Systems*, 7–11.

Bot, P., Viola, I.M., Flay, R.G., and Brett, J.S. (2014). Wind-tunnel pressure measurements on model-scale rigid downwind sails. *Ocean Engineering*, 90, 84–92.

Burns, J.A. and Herdman, T.L. (2021). Optimal sensor placement for observer design. *IFAC-PapersOnLine*, 54(9), 446–451.

Byrd, R.H., Hribar, M.E., and Nocedal, J. (1999). An interior point algorithm for large-scale nonlinear programming. *SIAM Journal on Optimization*, 9(4), 877–900.

Cecilia, A. and Costa-Castelló, R. (2021). On state-estimation in weakly-observable scenarios and implicitly regularized observers. In *2021 60th IEEE Conference on Decision and Control (CDC)*, 3996–4001.

Dupuy, D., Toutant, A., and Bataille, F. (2020). Analysis of artificial pressure equations in numerical simulations of a turbulent channel flow. *Journal of Computational Physics*, 411, 109407.

Georges, D. (2025). Wildfire mitigation using an aerial firefighting vehicle: An optimal control approach. In *Proceedings of the IEEE Conference on Decision and Control (CDC)*. To appear.

Kumar, P., El Sayed, Y.M., and Semaan, R. (2014). Optimized sensor placement using stochastic estimation for a flow over a 2D airfoil with coanda blowing. In *7th AIAA Flow Control Conference*, 2101.

Le Pelley, D., Morris, D., Richards, P., and Motta, D. (2012). Aerodynamic force deduction on yacht sails using pressure and shape measurements in real time. In *4th High Performance Yacht Design Conference*, 28–37.

Luenberger, D.G. (1971). An introduction to observers. *IEEE Transactions on Automatic Control*, 16(6), 596–602. doi:10.1109/TAC.1971.1099826.

Meinicke, A.C. and Cesnik, C. (2025). Observability-based sensor selection and dimensionality reduction of pressure distribution for a vehicle-as-a-sensor concept. In *AIAA SCITECH 2025 Forum*, 2269.

Rossetti, A., Codeluppi, R., Golfarelli, A., Zagnoni, M., Talamelli, A., and Tartagni, M. (2011). Design and characterization of polymeric pressure sensors for wireless wind sail monitoring. *Sensors and actuators A: Physical*, 167(2), 162–170.

Seth, G., Bhushan, M., and Patwardhan, S.C. (2024). Optimal sensor placement design for profile estimation of distributed parameter systems. *Industrial & Engineering Chemistry Research*, 63(9), 4046–4067.

Summers, T.H. and Lygeros, J. (2014). Optimal sensor and actuator placement in complex dynamical networks. *IFAC Proceedings Volumes*, 47(3), 3784–3789.

Sun, S., Liu, S., Chen, M., and Guo, H. (2019). An optimized sensing arrangement in wind field reconstruction using CFD and POD. *IEEE Transactions on Sustainable Energy*, 11(4), 2449–2456.

Tipsuwan, Y., Sanposh, P., and Techajaroonjit, N. (2023). Overview and control strategies of autonomous sailboats—a survey. *Ocean Engineering*, 281, 114879.

Toutant, A. (2017). General and exact pressure evolution equation. *Physics Letters A*, 381(44), 3739–3742.

Toutant, A. (2018). Numerical simulations of unsteady viscous incompressible flows using general pressure equation. *Journal of Computational Physics*, 374, 822–842.

Viola, I., Bot, P., and Riotte, M. (2013). Upwind sail aerodynamics: A RANS numerical investigation validated with wind tunnel pressure measurements. *International Journal of Heat and Fluid Flow*, 39, 90–101.

Wrobel, M. and Meurer, T. (2021). Optimal sensor placement for temperature control in a deep drawing tool. *IFAC-PapersOnLine*, 54(11), 91–96.

Zhang, Y., Zhang, S., Jiang, F., Wu, Z., and Li, W. (2025). Predicting surface pressure fields and lift coefficients of subsonic airfoils by machine-learning-enhanced compressive sensing framework. *Physics of Fluids*, 37(9).

Zhou, K., Zhou, L., Zhao, S., Qiang, X., Liu, Y., and Wen, X. (2021). Data-driven method for flow sensing of aerodynamic parameters using distributed pressure measurements. *AIAA Journal*, 59(9), 3504–3516.

Appendix A. PROOF OF THEOREM 1

Consider the estimation error $e(\boldsymbol{\eta},t)\in C^1([0,\infty);L^2(\Omega))$ and the Lyapunov function

$$V(t)=\frac{\beta_0}{2}\iint_\Omega e^2(\boldsymbol{\eta},t)\,d\boldsymbol{\eta}. \tag{A.1}$$

Taking the time derivation of (A.1) along the trajectories of the observer error dynamics (7) yields

$$\begin{aligned}\dot V(t)=\beta_0 a_p\iint_\Omega e(\boldsymbol{\eta},t)(\partial_{ss}e(\boldsymbol{\eta},t)+\partial_{zz}e(\boldsymbol{\eta},t))\,d\boldsymbol{\eta}\\ -\sum_{i=1}^{n}\sum_{j=1}^{m}\bar k_{ij}e^2(\bar{\boldsymbol{\eta}}_{ij},t)-\sum_{i=1}^{n}\sum_{j=1}^{m}\bar k_{ij}e(\bar{\boldsymbol{\eta}}_{ij},t)g_{ij}(t),\end{aligned} \tag{A.2}$$

where $\bar k_{ij}=\beta_0 k_{ij}$ and the sifting property of the Dirac delta function was used for the last term. Assume that the measurement disturbance is bounded such that

$$|g_{ij}(t)|\le g_{\max},\quad \forall\, t\ge 0,\ \forall\, i,j. \tag{A.3}$$

Applying Young's inequality $ab\le\frac{\kappa}{2}a^2+\frac{1}{2\kappa}b^2$ to the cross term $e(\bar{\boldsymbol{\eta}}_{ij},t)g_{ij}(t)$ with $\kappa\in(0,2)$, and applying integration by parts to the diffusive terms together with the Dirichlet boundary conditions from (7), gives

$$\begin{aligned}\dot V(t)\le&-\beta_0 a_p\iint_\Omega\partial_s e^2(\boldsymbol{\eta},t)\,d\boldsymbol{\eta}-\beta_0 a_p\iint_\Omega\partial_z e^2(\boldsymbol{\eta},t)\,d\boldsymbol{\eta}\\ &-\sum_{i=1}^{n}\sum_{j=1}^{m}\bar k_{ij}\big(1-\frac{\kappa}{2}\big)e^2(\bar{\boldsymbol{\eta}}_{ij},t)+C_g,\end{aligned} \tag{A.4}$$

where $C_g=\sum_{i=1}^{n}\sum_{j=1}^{m}\frac{\bar k_{ij}}{2\kappa}g_{\max}^2$, and the condition $\kappa\in(0,2)$ ensures that the sensor feedback term remains strictly dissipative. Considering $\bar s_i\in[s_i,s_{i+1}]$ and $\bar z_j\in[z_j,z_{j+1}]$, define the local deviations

$$\begin{cases}\tilde e_i(\boldsymbol{\eta},t)=e(\boldsymbol{\eta},t)-e(\bar s_i,z,t)\\ \tilde e_j(\boldsymbol{\eta},t)=e(\boldsymbol{\eta},t)-e(s,\bar z_j,t),\end{cases} \tag{A.5}$$

so that $\tilde e_i(\bar s_i,z,t)=\tilde e_j(s,\bar z_j,t)=0$, and $\partial_s\tilde e_i(\boldsymbol{\eta},t)=\partial_s e(\boldsymbol{\eta},t)$, $\partial_z\tilde e_j(\boldsymbol{\eta},t)=\partial_z e(\boldsymbol{\eta},t)$ on their respective subdomains. Using Wirtinger's inequality on each subdomain $(s_i,s_{i+1})\times(z_j,z_{j+1})$ gives

$$\begin{aligned}&-\beta_0 a_p\sum_{j=1}^{m}\sum_{i=1}^{n}\int_{z_j}^{z_{j+1}}\int_{s_i}^{s_{i+1}}\partial_s e^2(\boldsymbol{\eta},t)\,ds\,dz\\ &=-\beta_0 a_p\sum_{j=1}^{m}\sum_{i=1}^{n}\int_{z_j}^{z_{j+1}}\Big(\int_{s_i}^{\bar s_i}+\int_{\bar s_i}^{s_{i+1}}\Big)\partial_s\tilde e_i^2(\boldsymbol{\eta},t)\,ds\,dz\\ &\le-\frac{\beta_0 a_p\pi^2}{4(\bar s_i-s_i)^2}\sum_{j=1}^{m}\sum_{i=1}^{n}\int_{z_j}^{z_{j+1}}\int_{s_i}^{\bar s_i}\tilde e_i^2(\boldsymbol{\eta},t)\,ds\,dz\\ &\quad-\frac{\beta_0 a_p\pi^2}{4(s_{i+1}-\bar s_i)^2}\sum_{j=1}^{m}\sum_{i=1}^{n}\int_{z_j}^{z_{j+1}}\int_{\bar s_i}^{s_{i+1}}\tilde e_i^2(\boldsymbol{\eta},t)\,ds\,dz\\ &\le-\frac{\beta_0 a_p\pi^2}{4\phi_i}\sum_{j=1}^{m}\sum_{i=1}^{n}\int_{z_j}^{z_{j+1}}\int_{s_i}^{s_{i+1}}\tilde e_i^2(\boldsymbol{\eta},t)\,ds\,dz,\end{aligned} \tag{A.6}$$

where $\phi_i=\max\{(\bar s_i-s_i)^2,(s_{i+1}-\bar s_i)^2\}$. Similarly,

$$\begin{aligned}&-\beta_0 a_p\sum_{j=1}^{m}\sum_{i=1}^{n}\int_{z_j}^{z_{j+1}}\int_{s_i}^{s_{i+1}}\partial_z e^2(\boldsymbol{\eta},t)\,ds\,dz\\ &\le-\frac{\beta_0 a_p\pi^2}{4\varphi_j}\sum_{j=1}^{m}\sum_{i=1}^{n}\int_{z_j}^{z_{j+1}}\int_{s_i}^{s_{i+1}}\tilde e_j^2(\boldsymbol{\eta},t)\,ds\,dz,\end{aligned} \tag{A.7}$$

with $\varphi_j=\max\{(\bar z_j-z_j)^2,(z_{j+1}-\bar z_j)^2\}$. Combining (A.5), (A.6), and (A.7) with (A.4), one obtains

$$\dot V(t)\le\sum_{j=1}^{m}\sum_{i=1}^{n}\int_{z_j}^{z_{j+1}}\int_{s_i}^{s_{i+1}}\mathbf{E}_{ij}^T\boldsymbol{\Psi}_{ij}\mathbf{E}_{ij}\;ds\,dz+C_g, \tag{A.8}$$

where $\mathbf{E}_{ij}=[e(\boldsymbol{\eta},t),\ e(\bar s_i,z,t),\ e(s,\bar z_j,t),\ e(\bar s_i,\bar z_j,t)]^T$ and $\boldsymbol{\Psi}_{ij}$ satisfying (8) ensures that $\dot V(t)\le C_g$.

For the LMI (8), there exists a constant $\varrho>0$ such that

$$\boldsymbol{\Psi}_{ij}+0.5\varrho\mathbf{I}\le 0,\ i\in\mathcal{I},\ j\in\mathcal{J}. \tag{A.9}$$

Substituting (A.9) into (A.8) gives

$$\begin{aligned}\dot V(t)&\le-0.5\varrho\sum_{j=1}^{m}\sum_{i=1}^{n}\int_{z_j}^{z_{j+1}}\int_{s_i}^{s_{i+1}}\mathbf{E}_{ij}^T\mathbf{E}_{ij}\;ds\,dz+C_g,\\ &\le-0.5\varrho\iint_\Omega e^2(\boldsymbol{\eta},t)\,d\boldsymbol{\eta}+C_g=-\frac{\varrho}{\beta_0}V(t)+C_g.\end{aligned} \tag{A.10}$$

Integrating (A.10) over $[0,t]$ gives

$$V(t)\le V(0)\exp\big(-\tfrac{\varrho}{\beta_0}t\big)+\frac{\beta_0 C_g}{\varrho}\big(1-\exp\big(-\tfrac{\varrho}{\beta_0}t\big)\big), \tag{A.11}$$

for $t\ge 0$, which by definition of $V(t)$ implies the exponential decay:

$$\begin{aligned}\|e(\cdot,t)\|_{L^2(\Omega)}\le\|e(\cdot,0)\|_{L^2(\Omega)}\exp\Big(-\tfrac{\varrho}{2\beta_0}t\Big)\\ +\sqrt{\frac{2C_g}{\varrho}\big(1-\exp\big(-\tfrac{\varrho}{\beta_0}t\big)\big)},\quad t\ge 0,\end{aligned} \tag{A.12}$$

where the ultimate bound is given in (10). Therefore, the closed-loop observer error system is input-to-state stable with respect to bounded measurement disturbances, with exponential decay to an ultimate bound in $L^2(\Omega)$. Matrix $\boldsymbol{\Psi}_{ij}$ can be expressed as

$$\boldsymbol{\Psi}_{ij}=\begin{bmatrix}\mathbf{M}_{ij} & \mathbf{0}\\ \mathbf{0}^T & -\frac{\bar k_{ij}(1-\frac{\kappa}{2})}{A_{ij}}\end{bmatrix},\ \mathbf{M}_{ij}=-\vartheta\begin{bmatrix}\alpha_i+\mu_j & -\alpha_i & -\mu_j\\ -\alpha_i & \alpha_i & 0\\ -\mu_j & 0 & \mu_j\end{bmatrix},$$

where $\alpha_i=\frac{1}{\phi_i}$ and $\mu_j=\frac{1}{\varphi_j}$. Condition (A.9), using the Schur complement, is equivalent to $\mathbf{M}_{ij}+\frac{\varrho}{2}\mathbf{I}\le 0$ and

$-\frac{\bar{k}_{ij}(1-\frac{\kappa}{2})}{A_{ij}}+\frac{\varrho}{2}\leq 0$. Matrix $\mathbf{M}_{ij}$ has eigenvalues $-\vartheta\{0,\ \alpha_i+\mu_j \pm \sqrt{\alpha_i^2-\alpha_i\mu_j+\mu_j^2}\}$, therefore, for each $i\in\mathcal{I},\ j\in\mathcal{J}$, the admissible ϱ must satisfy

$$\varrho_{ij}^{\max}=2\,\min\left\{\vartheta\Big(\alpha_i+\mu_j-\sqrt{\alpha_i^2-\alpha_i\mu_j+\mu_j^2}\Big),\ \frac{\bar{k}_{ij}(1-\frac{\kappa}{2})}{A_{ij}}\right\}. \quad \text{(A.13)}$$

The global decay rate is then $\varrho^\star=\min\{\varrho_{ij}^{\max}\}$. Choosing any $0<\varrho<\varrho^\star$ ensures the inequality in (A.9) holds, which completes the proof.

Appendix B. PROOF OF THEOREM 2

This section presents the computation of the Gâteaux derivatives of the Lagrangian (14) necessary to establish the first-order optimality conditions (15), (16), and (17). After performing the required integrations by parts, once in time and three times in space, the Lagrangian in (14) can be written in its weak form as

$$\begin{aligned}\mathcal{L}=&\frac{q_1}{2}\int_0^{T_f}\iint_\Omega e^2(\boldsymbol{\eta},t)\,d\boldsymbol{\eta}\,dt+\frac{q_2}{2}\sum_{i=1}^{n}\sum_{j=1}^{m}\|\bar{\boldsymbol{\eta}}_{ij}-\bar{\boldsymbol{\eta}}_{ij}^{d}\|_2^2\\&-\int_0^{T_f}\iint_\Omega\partial_t\lambda(\boldsymbol{\eta},t)e(\boldsymbol{\eta},t)\,d\boldsymbol{\eta}\,dt\\&+\iint_\Omega[\lambda(\boldsymbol{\eta},T_f)e(\boldsymbol{\eta},T_f)-\lambda(\boldsymbol{\eta},0)e(\boldsymbol{\eta},0)]\,d\boldsymbol{\eta}\\&-a_p\int_0^{T_f}[\lambda(\boldsymbol{\eta},t)\partial_{\boldsymbol{\eta}}e(\boldsymbol{\eta},t)]_{\partial\Omega}\,dt\\&-a_p\int_0^{T_f}\iint_\Omega\partial_{\boldsymbol{\eta}\boldsymbol{\eta}}\lambda(\boldsymbol{\eta},t)e(\boldsymbol{\eta},t)\,d\boldsymbol{\eta}\,dt\\&+a_p\int_0^{T_f}[\partial_{\boldsymbol{\eta}}\lambda(\boldsymbol{\eta},t)e(\boldsymbol{\eta},t)]_{\partial\Omega}\,dt\\&+\int_0^{T_f}\iint_\Omega\left(\lambda(\boldsymbol{\eta},t)\boldsymbol{c}^T(\boldsymbol{\eta})\boldsymbol{K}\iint_\Omega\boldsymbol{c}(\boldsymbol{\xi})e(\boldsymbol{\xi},t)\,d\boldsymbol{\xi}\right)d\boldsymbol{\eta}\,dt,\end{aligned} \quad \text{(B.1)}$$

where $[\cdot]_{\partial\Omega}$ denotes boundary transversality contributions. For a rectangular domain $\Omega=[0,L_s]\times[0,L_z]$, the boundary terms explicitly expand as

$$\begin{aligned}&\int_0^{T_f}[\lambda(\boldsymbol{\eta},t)\partial_{\boldsymbol{\eta}}e(\boldsymbol{\eta},t)]_{\partial\Omega}\,dt=\\&\int_0^{T_f}[\lambda(L_s,z,t)\partial_s e(L_s,z,t)-\lambda(0,z,t)\partial_s e(0,z,t)]\,dt\\&+\int_0^{T_f}[\lambda(s,L_z,t)\partial_z e(s,L_z,t)-\lambda(s,0,t)\partial_z e(s,0,t)]\,dt,\end{aligned} \quad \text{(B.2)}$$

and analogous expressions hold for the remaining boundary terms.

The Gâteaux derivatives of $\mathcal{L}$ with respect to e, $\bar{s}_i$, and $\bar{z}_j$ are now computed to search for the optimality conditions. Consider the first variation of (B.1) with respect to e, for Dirichlet boundary conditions $\lambda(\boldsymbol{\eta},t)\big|_{\partial\Omega}=0$, and an arbitrary admissible perturbation δe:

$$\begin{aligned}D_e\mathcal{L}[e;\delta e]=&\int_0^{T_f}\iint_\Omega q_1e(\boldsymbol{\eta},t)\delta e(\boldsymbol{\eta},t)\,d\boldsymbol{\eta}\,dt\\&-\int_0^{T_f}\iint_\Omega\partial_t\lambda(\boldsymbol{\eta},t)\delta e(\boldsymbol{\eta},t)\,d\boldsymbol{\eta}\,dt\\&+\iint_\Omega[\lambda(\boldsymbol{\eta},T_f)\delta e(\boldsymbol{\eta},T_f)-\lambda(\boldsymbol{\eta},0)\delta e(\boldsymbol{\eta},0)]\,d\boldsymbol{\eta}\\&-a_p\int_0^{T_f}\iint_\Omega\partial_{\boldsymbol{\eta}\boldsymbol{\eta}}\lambda(\boldsymbol{\eta},t)\delta e(\boldsymbol{\eta},t)\,d\boldsymbol{\eta}\,dt\\&+\int_0^{T_f}\iint_\Omega\delta e(\boldsymbol{\eta},t)\left(\boldsymbol{c}^T(\boldsymbol{\eta})\boldsymbol{K}\iint_\Omega\boldsymbol{c}(\boldsymbol{\xi})\lambda(\boldsymbol{\xi},t)\,d\boldsymbol{\xi}\right)d\boldsymbol{\eta}\,dt,\end{aligned} \quad \text{(B.3)}$$

where $D_e\mathcal{L}[e;\delta e]$ denotes the Gâteaux derivative of $\mathcal{L}$ with respect to e in the direction of δe. The perturbations satisfy the homogeneous variations $\delta e(\boldsymbol{\eta},0)=0$ for all $\boldsymbol{\eta}\in\Omega$ and $\delta e(\boldsymbol{\eta},t)=0$ for all $\boldsymbol{\eta}\in\partial\Omega$, reflecting the fixed initial condition and Dirichlet boundary conditions. Using $\lambda(\boldsymbol{\eta},T_f)=0$, and imposing the stationary condition $D_e\mathcal{L}[e;\delta e]=0$ then yields the optimal system governing the coupled state and adjoint equation in (15).

Considering variations in the sensor location $\bar{s}_i$ (the $\bar{z}_j$ case is analogous), the Gâteaux derivative in the direction $\delta\bar{s}_i$ is

$$\begin{aligned}&D_{\bar{s}_i}\mathcal{L}[\bar{s}_i;\delta\bar{s}_i]=\\&\int_0^{T_f}\iint_\Omega\Big[-q_1e(\boldsymbol{\eta},t)+\partial_t\lambda(\boldsymbol{\eta},t)+a_p\partial_{\boldsymbol{\eta}\boldsymbol{\eta}}\lambda(\boldsymbol{\eta},t)\\&-\boldsymbol{c}^T(\boldsymbol{\eta})\boldsymbol{K}\iint_\Omega\boldsymbol{c}(\boldsymbol{\xi})\lambda(\boldsymbol{\xi},t)\,d\boldsymbol{\xi}\Big]\partial_{\bar{s}_i}\hat{\bar{p}}(\boldsymbol{\eta},t)\delta\bar{s}_i\,d\boldsymbol{\eta}\,dt\\&+k_{ij}\int_0^{T_f}\iint_\Omega e(\boldsymbol{\eta},t)\Big[\partial_{\bar{s}_i}c_{ij}(\boldsymbol{\eta})\iint_\Omega c_{ij}(\boldsymbol{\xi})\lambda(\boldsymbol{\xi},t)\,d\boldsymbol{\xi}\\&+c_{ij}(\boldsymbol{\eta})\iint_\Omega\partial_{\bar{s}_i}c_{ij}(\boldsymbol{\xi})\lambda(\boldsymbol{\xi},t)\,d\boldsymbol{\xi}\Big]\delta\bar{s}_i\,d\boldsymbol{\eta}\,dt\\&+q_2(\bar{s}_i-s_{d,i})\delta\bar{s}_i.\end{aligned} \quad \text{(B.4)}$$

Substituting the adjoint system (15) into (B.4), and imposing the stationary condition $D_{\bar{s}_i}\mathcal{L}[\bar{s}_i;\delta\bar{s}_i]=0$ provides the optimal sensor-location condition in (16), with $\bar{z}_j$ obtained similarly in (17).